

Tunneling-Induced Deformation of Bare Frame Structures on Sand: Numerical Study of Building Deformations

D. Boldini¹; N. Losacco²; A. Franza³; M. J. DeJong⁴; J. Xu⁵; and A. M. Marshall⁶

Abstract: The paper compares the performance of two FEM approaches in reproducing the response of bare frame structures to tunneling in dry dense sand. A fully coupled approach, in which the tunnel, frame, and soil are accounted for, is compared with a two-stage method incorporating simpler structural and soil models. The two approaches are validated against centrifuge test results of tunneling in sand beneath frames founded on either rafts or separate footings. Both approaches provide good estimates of displacements and distortions experienced by the frames provided that the soil-foundation interface and structural stiffness are correctly accounted for. The numerical models are also employed to extend the range of eccentric configurations investigated with centrifuge tests. The results demonstrate that shear deformations play an important role for all considered buildings, whereas only frames on separate footings are sensitive to horizontal ground movements. Finally, data are synthesized using modification factors and recently proposed relative stiffness terms. DOI: [10.1061/\(ASCE\)GT.1943-5606.0002627](https://doi.org/10.1061/(ASCE)GT.1943-5606.0002627). © 2021 American Society of Civil Engineers.

4 Introduction

The increasing need for efficient and high-capacity transportation systems in urban areas is boosting the construction of new tunnels worldwide. Modern mechanized excavation techniques, such as those based on closed-face TBMs with pressurized shields, usually limit tunneling-induced soil deformations and, consequently, the potential damage to structures and services, both above-ground and buried. However, problems can arise in the case of unexpected stratigraphic changes, technical malfunctioning or errors in TBM driving, hence consideration of more conservative scenarios of TBM performance is recommended for the sake of safety. In addition, traditional excavation techniques, generally associated with larger volume losses, are unavoidable in specific scenarios, e.g., for connection or platform tunnels.

In the context of tunnel-soil-building interactions, reliable predictive models are essential for optimum design. Compared to commonly employed simplified and often overconservative approaches, interaction models should provide more accurate predictions of the ground response at different levels of volume loss,

accounting explicitly for the characteristics of the buildings, including their foundation system and possible material nonlinearity.

For risk assessments, the first level of investigation typically consists of a two-step uncoupled assessment of the interaction problem (Mair et al. 1996): first, the greenfield response is calculated by adopting one of the available semiempirical expressions for ground displacements (Mair et al. 1993), and then, the structural damage is evaluated with reference to specific greenfield deformation or displacement parameters calculated at the foundation level of the building (Burland et al. 1977; Boscardin and Cording 1989). A more refined evaluation, needed if the category of damage resulting from this preliminary evaluation is not negligible, requires a coupled soil-structure interaction analysis in which the building can be modeled with various levels of detail, ranging from equivalent beams or solids representing the whole structure (Potts and Addenbrooke 1997; Namazi and Mohamad 2013; Losacco et al. 2016) to a more or less detailed description of the structural components (Son and Cording 2005; Comodromos et al. 2014; Fargnoli et al. 2015a; Yiu et al. 2017). In most cases, studies are conducted with the aid of numerical modeling, often in three dimensions so as to accurately describe the structural layout of the building and its relative orientation with respect to the tunnel axis.

Compared to masonry buildings, relatively little attention has been devoted to the response of framed structures to tunneling. The peculiar response of framed buildings to excavations (Goh and Mair 2014; Fargnoli et al. 2015b; Haji et al. 2018; Boldini et al. 2018; Fu et al. 2018) raises the need for specific damage criteria, accounting for the frame geometry (Boone 1996; Elkayam and Klar 2019) and for the predominant contribution of floors and walls to bending and shear stiffness respectively (Finno et al. 2005), as discussed in the next paragraph.

This paper aims at validating two different finite element (FE) approaches for the assessment of tunneling-induced deformation of framed structures with no or very compliant infills and the possible resulting damage on the latter, even if not explicitly modeled. Reference is made to an experimental database from recently performed centrifuge tests at the University of Nottingham, which evaluated the response of frames with varying geometry, foundation layout, stiffness, and weight to the excavation of a tunnel in dry, dense sand (Xu et al. 2020, 2021). The performance of an

¹Dept. of Chemical Engineering Materials Environment, Sapienza Univ. of Rome, Rome, Italy (corresponding author). ORCID: <https://orcid.org/0000-0001-7423-043X>. Email: daniela.boldini@uniroma1.it

²Dept. of Civil, Environmental, Land, Building Engineering and Chemistry, Polytechnic Univ. of Bari, Bari, Italy.

³Dept. of Civil and Architectural Engineering, Aarhus Univ., Aarhus, Denmark.

⁴Dept. of Civil and Environmental Engineering, Univ. of California, Berkeley, CA. ORCID: <https://orcid.org/0000-0002-6195-839X>

⁵Institute of Geotechnical Engineering, School of Transportation, Southeast Univ., Nanjing, China; formerly, Dept. of Civil Engineering, Univ. of Nottingham, Nottingham, UK. ORCID: <https://orcid.org/0000-0002-5814-247X>

⁶Dept. of Civil Engineering, Univ. of Nottingham, Nottingham, UK. ORCID: <https://orcid.org/0000-0003-1583-1619>

Note. This manuscript was submitted on June 26, 2020; approved on June 3, 2021. **No Epub Date**. Discussion period open until 0, 0; separate discussions must be submitted for individual papers. This paper is part of the *Journal of Geotechnical and Geoenvironmental Engineering*, © ASCE, ISSN 1090-0241.

73 advanced fully coupled FE numerical model, containing all the
 74 components of the interaction problem (i.e., the tunnel, the soil,
 75 and the frame), is compared to that of a simplified two-stage FE
 76 model. Results highlight the limitations and strengths of the two
 77 numerical modeling approaches, providing useful guidance to
 78 engineering practitioners. The numerical analyses are also used
 79 to extend the scope of investigation beyond that considered exper-
 80 imentally, by simulating further eccentric configurations and pro-
 81 viding further insight on the horizontal strains associated with
 82 differential displacements of buildings with separate footings.

83 In this paper, a review of the available methods for the assessment
 84 of deformation and damage of framed buildings is first presented,
 85 involving the estimation of a relative stiffness of the frame with re-
 86 spect to that of the soil. Next, the experimental campaign in sandy
 87 soil used as a comparison term is described. This is followed by the
 88 description of the numerical approaches and of the strategy adopted
 89 for parameter calibration. Finally, numerical results are compared
 90 to experimental data in terms of soil and frame displacements;
 91 the angular distortion and differential horizontal displacements,
 92 deemed the most appropriate indicator of frame deformation and
 93 expected damage of infills, if any, and their modification factors
 94 are summarized.

95 Assessment of Tunneling-Induced Structural 96 Deformations

97 The assessment of the potential tunneling-related damage of build-
 98 ings requires a careful evaluation of the induced deformation field.
 99 In the well-established Critical Strain method (Boscardin and
 100 Cording 1989), the maximum tensile strain ε_{\max} in any portion
 101 of the building—i.e., either a structural partition such as a bay or
 102 panel, or any part subject to a specific deformation mode, such
 103 as sagging/hogging or predominantly shear/bending—is associ-
 104 ated with a damage category, ranging from “negligible” to “very
 105 severe.” The ε_{\max} results from the composition of horizontal
 106 strains ε_h , induced by horizontal displacements, with either horizontal
 107 (bending) strains ε_b or diagonal (shear) strains ε_d induced by the
 108 vertical displacement field.

109 Traditionally, horizontal strains ε_h are inferred from the dis-
 110 placements measured at the ground surface or at the foundation
 111 level, while the bending and shear strains ε_b and ε_d are related
 112 to either the deflection ratio Δ/L (Burland and Wroth 1974) or
 113 the angular distortion β (Boscardin and Cording 1989), as defined
 114 **8** in Fig. 1. Recently, moving from Cook (1994), Ritter et al. (2020)
 115 proposed that the deformation parameters of the bay (both average
 116 curvature and shear strain) could be inferred from its top and
 117 bottom corner displacements, consistent with Xu et al. (2020).
 118 More specifically, for framed structures with continuous founda-
 119 tions (e.g., rafts, grade beams transverse to the tunnel), the shear
 120 deformation ε_d is typically dominant, because longitudinal strains
 121 due to ε_h and ε_b are negligible. The average shear strain level is
 122 given by the angular distortion $\beta = S - w$ of each panel or bay,
 123 as shown in Fig. 1, defined as the difference between the bay slope
 124 S and tilt w given by the rotation of the bay edges (Boone 1996);
 125 the angular distortion relates to the diagonal strain as $\varepsilon_d = \beta/2$. For
 126 separate footings, both shear and horizontal distortions need to
 127 be considered when estimating the panel or bay deformation; in
 128 this case, the maximum strain can be approximated from a Mohr’s
 129 circle for plane strain conditions (Mair et al. 1996) by

$$\varepsilon_{\max} = \frac{\varepsilon_h + \varepsilon_z}{2} + \sqrt{\left(\frac{\varepsilon_h - \varepsilon_z}{2}\right)^2 + \varepsilon_d^2} \quad (1)$$

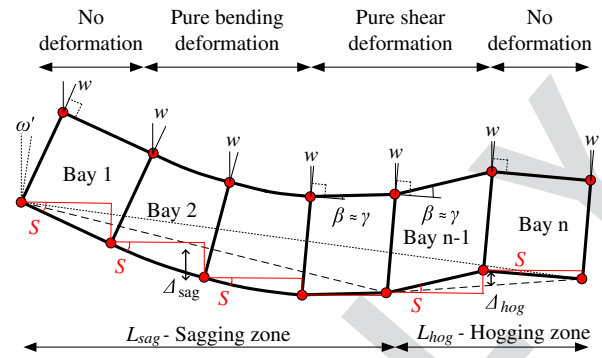


Fig. 1. Building deformation parameters inferred from bay corner displacements.

F1:1
 F1:2

where ε_h and ε_z = horizontal and vertical strains, respectively. Note **9** that ε_z may be neglected as a first approximation due to the axial
 130 action of columns restraining vertical deformations. Alternatively,
 131 vertical, horizontal, and diagonal strains may be computed directly
 132 from corner point displacements of flexible infills within bare
 133 frames (Elkayam and Klar 2019).
 134

135 The effect of the relative soil-structure stiffness in decreasing the
 136 distortions with respect to those evaluated in greenfield conditions
 137 was first introduced by Potts and Addenbrooke (1997) in terms of
 138 modification factors of Δ/L and ε_h for both sagging and hogging.
 139 Later, Son and Cording (2005) normalized the angular distortions
 140 of masonry building bays with respect to the differential ground
 141 slope obtained in greenfield conditions. By considering that framed
 142 configurations with axially stiff slabs/beams in the horizontal direc-
 143 tion undergo minimal longitudinal deformations (Finno et al. 2005)
 144 and thus shear deformation is dominant, Xu et al. (2020) introduced
 145 the angular distortion modification factor M^β and related it to a
 146 relative soil-structure stiffness parameter κ . The latter was defined
 147 as $\kappa = E_s B / GA_s^* = E_s B L / GA_s$, where E_s is the representative
 148 Young’s modulus of the soil, B is the building transverse length,
 149 L is the length of the building in the tunnel direction, and $GA_s^* =$
 150 GA_s / L is the building shear stiffness per meter run, where G is the
 151 shear modulus and A_s is the shear area contributing to shear resis-
 152 tance, which is only a portion of the cross-sectional area A (Cowper
 153 1966). The angular distortion modification $M^\beta = \beta_{\max} / \overline{GS}_{\max}$ is
 154 the ratio between the maximum angular distortion of the building
 155 β_{\max} and the maximum average greenfield slope \overline{GS}_{\max} , both de-
 156 fined with respect to the building bays. When $M^\beta = 1$, the framed
 157 building undergoes maximum shear deformations equal to the larg-
 158 est greenfield slope. It should be self-evident that the reliable
 159 application of this approach, or other similar methods, requires the
 160 implementation of rational procedures to estimate representative
 161 values of soil and structure stiffness.
 162

163 Finally, a modification factor for compressive and tensile
 164 horizontal strains between separate footings, caused by horizon-
 165 tal ground movements, is also considered. This is defined as
 166 $M^{\varepsilon_h} = \varepsilon_{h,\max}^{bld} / \varepsilon_{h,\max}^{gf}$, where $\varepsilon_{h,\max}^{bld}$ is the maximum horizontal strain
 167 at the building foundation and $\varepsilon_{h,\max}^{gf}$ is the largest average strain
 168 inferred from the greenfield displacements at the footing locations
 169 (Dimmock and Mair 2008). The relative structure-soil stiffness is
 170 inferred from an analysis of the response of a single portal, with
 171 one story and a single bay, to a differential horizontal displace-
 172 ment (Goh and Mair 2014). This approach provides the dimension-
 173 less factor $\alpha_f^* = 1 / (EsL) \times 3K_b K_c / (h_{story}^2 (2K_b + 3K_c))$, where
 174 $K_c = EI_c / h_{story}$ and $K_b = EI_b / b_{bay}$, EI_c and EI_b are the bending

Table 1. Configuration of numerically simulated centrifuge tests

Label	Foundation type	# stories	# bays	Centrifuge scale (dimension in mm)				Prototype (dimension in m)					
				t	H	B	b_{bay}	t	H	B	b_{bay}	e/B	
T1:2													
T1:3	Raft	5	6	4.8	195.3	462.0	76.2	0.32	13.3	31.4	5.2	0	
T1:4	Raft	2	6	4.8	81.0	462.0	76.2	0.32	5.5	31.4	5.2	0	
T1:5	Raft and separate footings	2	6	3.2	79.4	460.4	76.2	0.22	5.4	31.3	5.2	0	
T1:6	Raft	2	3	3.2	79.4	460.4	152.4	0.22	5.4	31.3	10.4	0	
T1:7	Raft and separate footings	2	3	3.2	79.4	231.8	76.2	0.22	5.4	15.8	5.2	0; 0.5	

Note: $h_{story} = 38.1$ mm at model scale and 2.6 m at prototype for all frames. For separate footings, $b_{foot} = 12$ mm at model scale and 0.8 m at prototype. All configurations modeled for standard (SW) and double self-weight (2SW).

175 stiffness of the column and the first-floor slabs, h_{story} is the column
176 height, and b_{bay} is the bay length.

$$\frac{\delta}{P} = b \frac{B^3}{\left(\frac{EI}{1+aF}\right)} \quad (2)$$

177 Representative Soil Stiffness

178 To evaluate a representative value of Young’s modulus for the soil
179 E_s , Mair (2013) suggested that the tunneling-induced level of shear
180 strain should be considered in combination with an appropriate soil
181 stiffness degradation curve. In this paper, the approach of Marshall
182 et al. (2010) and Farrell (2010) is adopted, considering ground
183 stresses and strains at middepth $z_t/2$, where z_t is the depth to
184 the tunnel axis.

185 Firstly, the soil stiffness degradation curve is acquired (i.e., the
186 relationship between the shear strain level γ_s and the relative reduction
187 of secant shear modulus G_s with respect to the initial “small-
188 strain” modulus G_0). The small-strain stiffness should be adjusted
189 to account for relative density and mean effective stress, e.g., using,
190 for example, the expressions proposed by Lehane and Cosgrove
191 (2000). Secondly, the average shear strain level γ_s experienced
192 by the soil during tunneling in greenfield conditions is evaluated
193 for a given tunnel volume loss $V_{l,t}$ (i.e., the relative change in tun-
194 nel cross-sectional area). To obtain γ_s , the shear strain distribution
195 at $z_t/2$ is averaged between $\pm 2.5i$, where i is the offset from
196 the tunnel centerline to the settlement trough inflection point.
197 Then, by assuming a value of Poisson’s ratio for the soil ν_s , the
198 representative value of the soil stiffness E_s is computed for any $V_{l,t}$.

199 Equivalent Frame Stiffness

200 Equivalent Timoshenko and laminated beams can be employed as a
201 simplified structural model, with the advantage of allowing separ-
202 ate control of the bending (EI) and shear (GA_s) contribution
203 (Finno et al. 2005; Pickhaver et al. 2010; Franza et al. 2020) to
204 the overall building stiffness. This approach can be contrasted with
205 that of the pure bending stiffness EI_{EB} based on the Euler-Bernoulli
206 beam theory (Franzius et al. 2006; Goh and Mair 2014; Haji et al.
207 2018). The equivalent bending and shear stiffness are typically esti-
208 mated by analytical methods (Franzius et al. 2006; Finno et al.
209 2005; Pickhaver et al. 2010) and loading tests, carried out either
210 experimentally or numerically (Son and Cording 2005; Xu et al.
211 2020; Losacco et al. 2014, 2016).

212 In this paper, the equivalent bending (EI) stiffness is analytically
213 obtained from the parallel axis theorem, using the cross-sectional
214 areas of the floor slabs. Next, the shear stiffness GA_s is estimated
215 from a loading test of a simply supported framed structure sub-
216 jected to a concentrated load, similar to Goh and Mair (2014).
217 For the Timoshenko beam theory, the deflection-to-force ratio
218 δ/P can be expressed as

219 where P = total applied force; B = beam length; and $F = (EI)/$
220 (B^2GA_s) . The adopted coefficients $a = 12$ and $b = 1/48$ depend
221 on the selected boundary conditions. It follows from Eq. (2) that
222 the shear stiffness GA_s is given by

$$\frac{1}{GA_s} = \frac{B^2}{aEI} \left(\frac{\delta}{P} \frac{EI}{bB^3} - 1 \right) \quad (3)$$

223 when using δ/P analytical estimated from a loading test and bending
224 stiffness EI .

225 This single equation approach based on Eq. (3) and the use of
226 the parallel axis theorem was validated against the shear stiffness
227 values obtained from multiple experimental loading tests carried
228 out by Xu et al. (2020, 2021). The single equation approach pre-
229 dicted slightly smaller (within 10%) stiffness values with respect to
230 the experiments. Therefore, using the parallel axis theorem to cal-
231 culate the equivalent EI with Eq. (3) is a reasonable approximation.

232 Description of Centrifuge Tests

233 In this paper, centrifuge tests of tunneling beneath a framed build-
234 ing are considered (Xu et al. 2020, 2021). At prototype scale, the
235 tunnel has diameter $D_t = 6.1$ m and a cover depth $C = 8$ m
236 ($C/D_t = 1.3$). For the frames, Table 1 provides details of the con-
237 sidered configurations and Fig. 2 shows the layout with an illus-
238 tration of relevant parameters. In this paper, frames are labeled

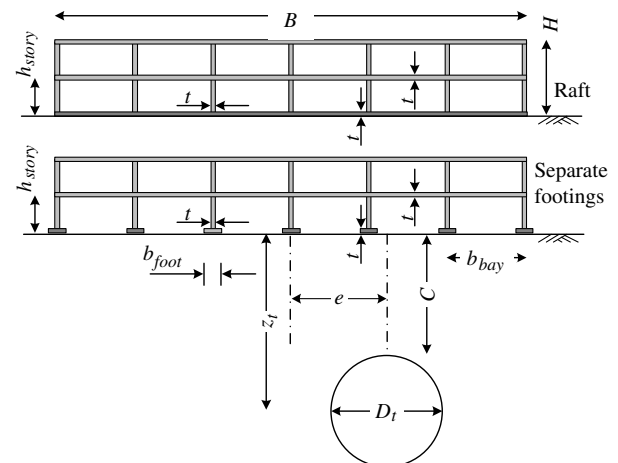


Fig. 2. Experimental layout for different tunnel-frame configurations.

239 following Xu et al. (2021) as $F_{xtybz}L$ or $F_{xtybz}S$: x is the number of
240 stories, y the thickness of structural elements at centrifuge model
241 scale, z is the number of bays, while L and S stands for long and
242 short building, respectively. Tunnel volume losses up to 3% were
243 considered, although most of the numerical results are reported for
244 $V_{l,t} = 1$ and 2%.

245 The experiments were performed at 68 times normal gravity
246 (68 g) and used a plane-strain setup. Within the strongbox, a flex-
247 ible cylindrical membrane filled with water simulates the tunnel;
248 excavation is reproduced by extracting a measured volume of water
249 from the membrane, thus controlling the tunnel volume loss. A dry
250 fine-grained silica sand, known as Leighton Buzzard Fraction E,
251 was used for the soil; this material is characterized by minimum
252 and maximum void ratios of 0.65 and 1.01, respectively. All con-
253 sidered experiments were performed with a soil relative density
254 $I_d = 90\%$, to which the numerical study exclusively refers. Triaxial
255 tests on this material were carried out by Zhao (2008) and Visone
256 (2008), data from which were used to evaluate soil representative
257 stiffness and calibrate the advanced numerical models, respectively
258 (details provided in a subsequent section).

259 Model frames were made of aluminum, consisting of vertical
260 walls and horizontal slabs that extended 258 mm in the longitudinal
261 tunnel direction, leaving a 1-mm gap between the frame and the
262 front/back strongbox walls. To achieve a rigid wall-slab connec-
263 tion, adjoining model frame parts were welded together along ap-
264 proximately 60% of the connected lengths (in the tunnel direction).
265 A layer of sand was glued to the base of the bottom slab to provide
266 a rough soil-raft foundation interface. After centrifuge testing with
267 the frame on raft foundation, the same model was modified to cre-
268 ate the separate footings configuration (by machining out portions
269 of the bottom slab). Note that the welding process did result in
270 some asymmetric response of the frame to loading, which will have
271 affected horizontal footing displacements in the centrifuge tests;
272 this was discussed in detail in Xu et al. (2021).

273 An experimental parametric study of the tunnel-frame interac-
274 tion problem was performed by varying the geometry, stiffness,
275 weight, foundation type, and eccentricity e of the structure with
276 respect to the tunnel centerline. As detailed in Table 1: the number
277 of stories was either 2 or 5; the number of bays was either 3 or 6; the
278 bay length was either 5.2 or 10.4 m (prototype scale), the latter for
279 the frame with 3 bays only; the thickness t of the structural elements
280 was either 0.32 or 0.22 m (prototype scale); the eccentricity to
281 frame width ratio, e/B , was either zero (“centered” cases) or 0.5
282 (“eccentric” cases); the weight of the frame was either its own
283 self-weight (indicated as SW) or double the self-weight (indicated
284 as 2SW), achieved by adding masses to the top of the frame in a
285 way that did not alter the structural stiffness. A total of 12 tests was
286 performed with frames on raft foundations, whereas 6 tests were
287 conducted for frames on separate footings, where the footing width
288 $b_{foot} = 0.8$ m (prototype scale).

289 Details of Numerical Modeling

290 In this section, the two FE approaches adopted for the numerical
291 investigation are described. The advanced numerical model re-
292 quires detailed information on soil behavior and structural char-
293 acteristics, along with associated requirements of computational
294 and postprocessing costs. On the other hand, the two-stage model
295 is suitable for quick preliminary estimates and sensitivity studies
296 because of the limited number of required inputs as well as its
297 negligible execution time.

298 The simulations with the advanced model were carried out more
299 or less simultaneously with the experimental campaign in the

centrifuge. The outcomes of the experiments were not known
and only the results of the loading tests on the frame were available
at the time; hence, the analyses can be considered as Class B pre-
dictions (Lambe 1973). The fully coupled modeling technique was
used to simulate all centrifuge tests in Table 1 (alternatively, see
Table S1). After verifying the accuracy of the predictions, the same
technique was then employed to explore the impact of tunnel-
building eccentricity on the deformations of the frame. Seven addi-
tional simulations were performed: frames F_{2t3b3L} and F_{2t3b6L}
founded on both footings and rafts for $e/B = 0.5$ and SW/2SW
weight conditions, except for the F_{2t3b3L} 2SW case on footings,
which did not converge.

The two-stage approach was employed to perform a Class A
prediction (i.e., before the experiment was carried out, but with
available experimental information on greenfield tunneling and its
effects on buildings in similar conditions) of the frame F_{2t3b6L} on
a raft foundation. Subsequently, the full set of analyses was per-
formed again after the centrifuge tests were completed (Class C
predictions), using the experimental greenfield data as an input.

Advanced Model

The advanced numerical model was set up using the commercial
FE software Abaqus (version 6.14). Given the problem geometry
and boundary conditions, plane strain analyses were carried out.
A sample FE mesh, for case F_{2t3b6L} with separate footings,
is shown by Fig. S1 in “Supplemental Materials.” First-order,
4-noded plane strain elements with full integration were adopted
for the soil, whereas second-order 8-noded elements with reduced
integration were used for the frame. Conventional boundary con-
ditions were applied: horizontal displacements prevented along the
sides; both vertical and horizontal displacements are prevented
along the base.

Regarding the simulation steps, a gravitational lithostatic stress
field was initially applied to the soil assuming a coefficient of earth
pressure at rest $K_0 = 0.5$. The self-weight of the frame was then
slowly activated in order to achieve equilibrium. A no-penetration,
Coulomb-friction contact law was enforced between the ground
surface and the foundation, assuming a coefficient of friction
 $\tan(\phi'_{cs})$, with $\phi'_{cs} = 32^\circ$ as the critical state friction angle of the
soil. Subsequently, tunnel excavation was simulated in a simplified
fashion by incrementally applying a prescribed displacement field
at the tunnel boundary after removing the soil elements (Cheng
et al. 2007). This technique has proven capable of achieving a real-
istic greenfield subsidence profile at the ground surface (Rampello
et al. 2012; Amorosi et al. 2014). The prescribed tunnel boundary
displacements, the magnitude of which depend on the target $V_{l,t}$,
were defined to obtain a homothetic contraction of the tunnel cross-
section centered on the tunnel invert.

The advanced constitutive model SANISAND (Dafalias and
Manzari 2004) was adopted to simulate the soil response from very
small- to medium-strain levels ($V_{l,t}$ as large as 3% was generally
reached in the numerical analyses). The calibration of material
parameters, reported in Table S2, was based on a mixed strategy,
considering experimental data of the Fraction E sand used in the cen-
trifuge tests, for similar relative densities. In particular, starting from
the values reported in Giardina et al. (2020), a calibration process
was carried out with reference to the laboratory tests performed
by Visone (2008), consisting of drained and undrained triaxial com-
pression and extension tests as well as resonant column and torsional
shear tests. The final set of values listed in “Supplemental Materials”
was obtained by performing a further parametric study on two
specific constants, i.e., h_0 , controlling the plastic modulus, and A_0 ,
governing the dilatancy law, aimed at reproducing the greenfield

362 tunneling-induced displacements presented in Farrell et al. (2014).
 363 This approach, i.e., calibrating numerical parameters based on the
 364 simulations of the greenfield boundary value problem, is believed
 365 to be more robust than only using results from element-scale laboratory
 366 tests. Indeed, Fig. S3 shows an excellent match between
 367 numerical and experimental results in terms of the relationship between
 368 tunnel volume loss $V_{l,t}$ and ground surface volume loss $V_{l,s}$
 369 (where $V_{l,s}$ is the area of the surface settlement trough divided by the
 370 nominal area of the tunnel cross-section).

371 For the frame, a simple linear elastic constitutive law was
 372 adopted with Young's modulus $E = 53.8$ GPa, Poisson's ratio
 373 $\nu = 0.334$, and unit weight $\gamma = 27$ kN/m³. The reduced value
 374 of E used for the aluminum frame, instead of the standard
 375 70 GPa, was selected to account for the partial welding of the frame
 376 components (described earlier); this value of E was found by
 377 simulating load-deflection tests carried out on the frames (Xu
 378 et al. 2020).

379 Simplified Model

380 The performance of the advanced model was compared to that of
 381 the simplified elasticity-based two-stage FE model called Analysis
 382 of Structural Response to Excavation (ASRE) (Franza and DeJong
 383 2019; Franza et al. 2020). The mechanical components of the
 384 model are described as follows (sketched in Fig. S2). The structure,
 385 incorporating both the superstructure and foundation, is modeled as
 386 a frame consisting of Euler-Bernoulli beam elements with geometry
 387 and material properties of the prototype building; the self-weight
 388 was simulated as line loads applied along the beam axes. The
 389 structure is founded on coupled elastic springs simulating the
 390 ground as an elastic half-space of Young's modulus E_s and
 391 Poisson's ratio ν_s . The effects of tunnel excavation are simulated
 392 through a set of equivalent forces applied to the springs that
 393 reproduce the ground movements observed in greenfield conditions.
 394 In other words, in elasticity-based two-stage methods, (1) greenfield
 395 movements are firstly estimated; and then (2) the soil-structure
 396 system is solved for the forces associated with these greenfield
 397 movements. It follows that two-stage methods are approximated in
 398 case of soil nonlinearity, while they provide an exact solution for
 399 linear elastic soil-structure systems.

400 Two types of simplified analyses were conducted: linear elastic,
 401 labeled EL, and elastoplastic EP. For the EP analyses, plastic
 402 sliders are located at the soil-foundation interface such that
 403 horizontal and vertical tensile forces are limited, capturing
 404 slipping and gap formation mechanisms. In the EP analyses,
 405 the self-weight of the structure needs to be applied prior to
 406 simulating the tunnel excavation. In the elastic EL analyses,
 407 a perfect soil-foundation compatibility condition was assumed
 408 by deactivating the sliders.

409 Numerical simulations were carried out before [i.e., Class A
 410 predictions (Lambe 1973)] and after (i.e., Class C predictions)
 411 the centrifuge tests. When selecting the plane frame model
 412 parameters, $E = 70$ GPa and 54 GPa were assumed for the Class
 413 A and Class C predictions, respectively, because the influence
 414 of incomplete welding was not accounted for prior to the
 415 experiments. Also, the length of the structure in the tunnel
 416 direction L was set equal to 10 m.

417 For the ground, a representative Young's modulus of $E_s = 45$
 418 MPa and a Poisson's ratio of $\nu_s = 0.3$ were assumed for the
 419 elastic half-space. For the plastic sliders, a friction coefficient
 420 corresponding to that of the soil at critical state (i.e., 32°)
 421 and zero tensile strength were used. Centrifuge results of
 422 greenfield tunneling reported by Farrell et al. (2014) and Xu
 423 et al. (2020) were used to define the inputs for Classes A
 424 and C simulations, respectively.

Results of the Advanced Model

Comparison between Numerical and Centrifuge Results: Ground Surface Displacements

425 Numerical results and centrifuge data are compared in this section
 426 in terms of tunneling-induced settlements U_z and horizontal
 427 displacements U_x at the ground surface (these latter shown in
 428 "Supplemental Materials" for the raft foundation case due to their
 429 negligible importance for this type of foundation). Figs. 3 and
 430 S4 show the settlements and horizontal displacements, respectively,
 431 for the raft foundation cases, while Figs. 4 and 5 relate to
 432 separate footings. The subplots are arranged from top to bottom
 433 with increasing relative structural stiffness. All the displayed
 434 results refer to a tunnel volume

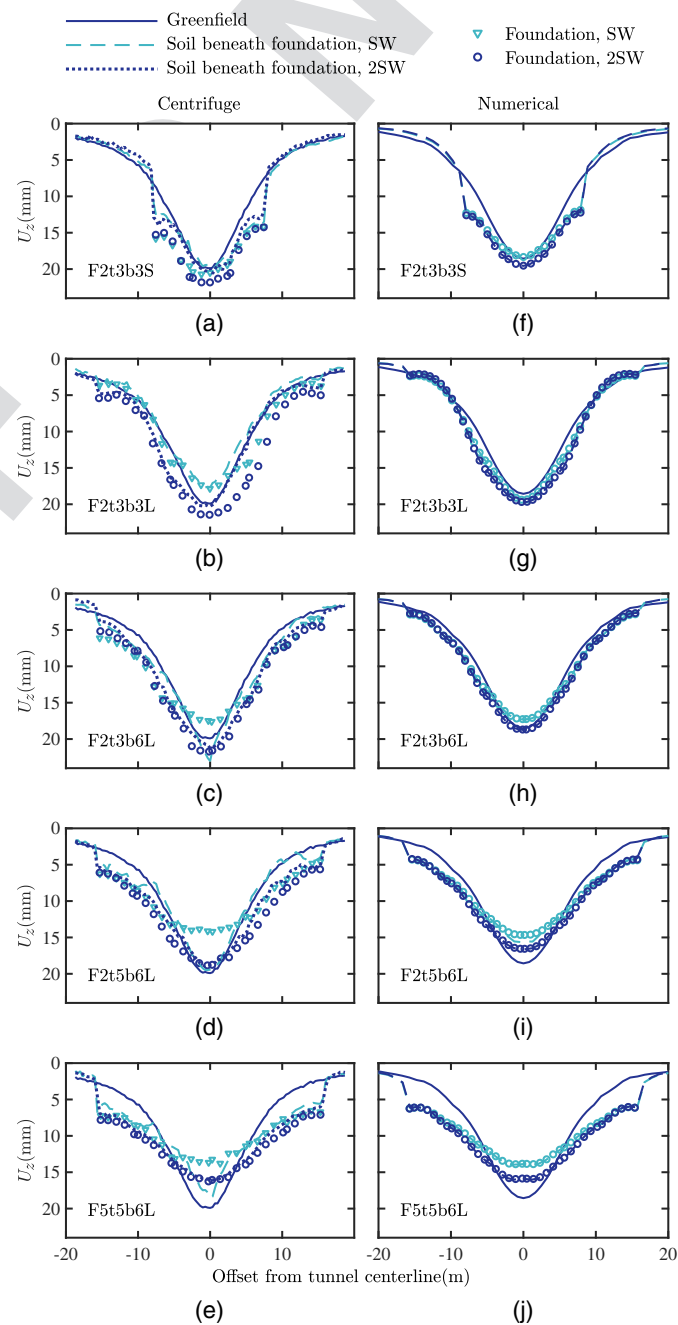


Fig. 3. Settlements of the raft foundations and underlying soil at $V_{l,t} = 1\%$: (a-e) centrifuge data; and (g-j) numerical results.

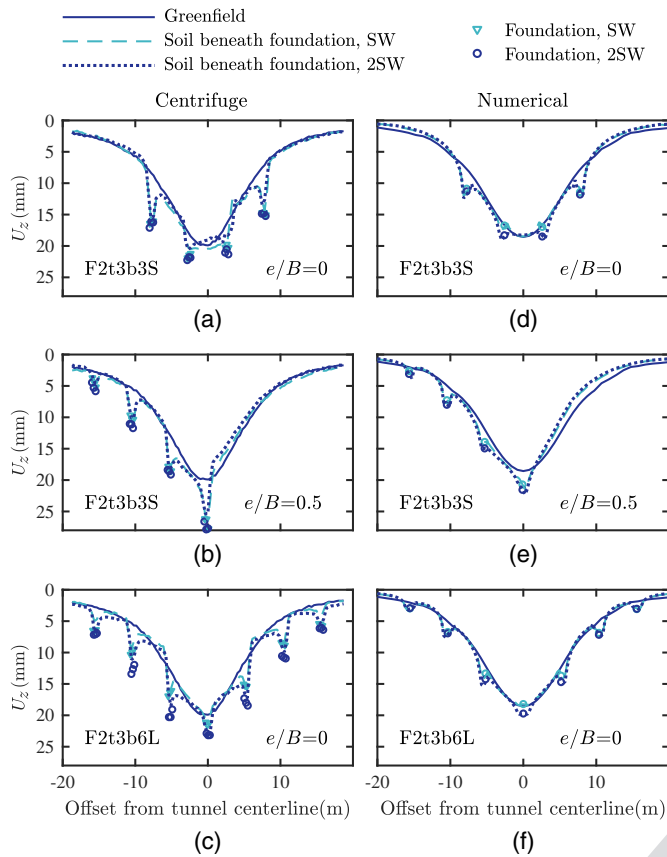


Fig. 4. Settlements of the separate footings and underlying soil at $V_{l,t} = 1\%$: (a–c) centrifuge data; and (d–f) numerical results.

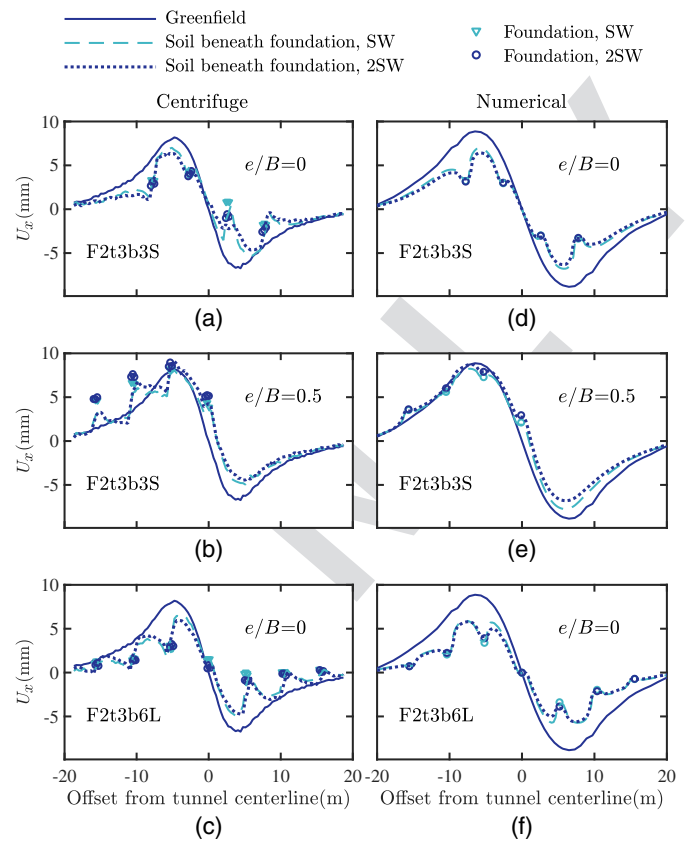


Fig. 5. Horizontal displacements of the separate footings and underlying soil at $V_{l,t} = 1\%$: (a–c) centrifuge data; and (d–f) numerical results.

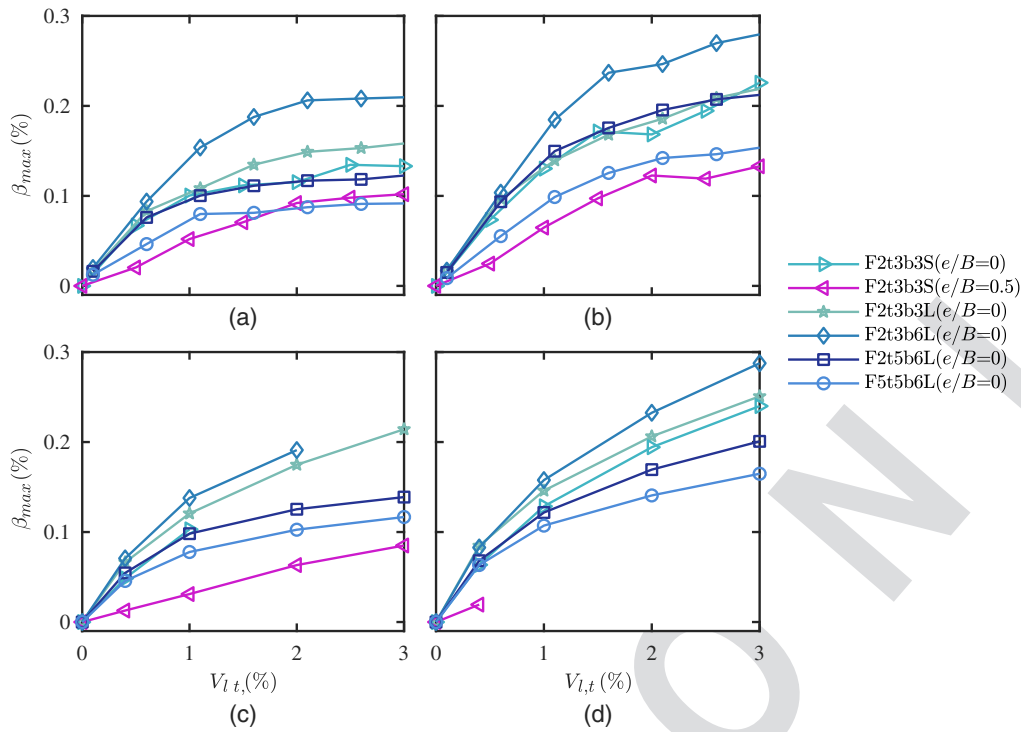
F4:1
F4:2

F5:1
F5:2

loss of 1%; for the sake of completeness, corresponding plots are provided in Figs. S5–S8 for a tunnel volume loss of 2%. The comparison in terms of settlements is generally good for frames founded on rafts (Fig. 3), but less good for frames on separate footings (Fig. 4). The centrifuge results indicate a gap between the underlying soil and the raft foundation for the three stiffer frames with nominal self-weight SW [Figs. 3(c–e), SW case]. Numerically, however, a gap was only detected for the raft-founded SW frames in test *F2t5b6L* for $V_{l,t} = 1\%$ [Fig. 6(i)] and in both tests *F2t5b6L* and *F5t5b6L* for $V_{l,t} = 2\%$ [Figs. S5(i and j)]. For frames on separate footings, a gap was not observed in the centrifuge nor in numerical results, even at $V_{l,t} = 2\%$ (see “Supplemental Materials”), though the numerical simulations tend to underestimate centrifuge test footing settlements. The influence of structural stiffness and weight on settlements is well captured by the numerical model for the raft foundation cases. Here, irrespective of the tunnel volume loss, the larger the frame stiffness, the smaller the maximum and differential settlements, which are also always smaller than in the greenfield case, at least for the long frame configurations. In the experiments, the additional applied weight (i.e., 2SW) was capable of remarkably altering the settlement distribution at the foundation level, particularly in the central portion of the structure. This behavior is reproduced only marginally, mainly for the stiffer frames, by the advanced FE simulations. Also, for frames with separate footings (Fig. 4), the computed FE settlement distribution appears only slightly affected by the frame stiffness at the global level, the response differing from that of the greenfield curve only locally, where the footings are located. The centrifuge data show more marked local settlements, especially for the eccentric case [Figs. 4(b) and S7(b)] for which much larger maximum settlements were

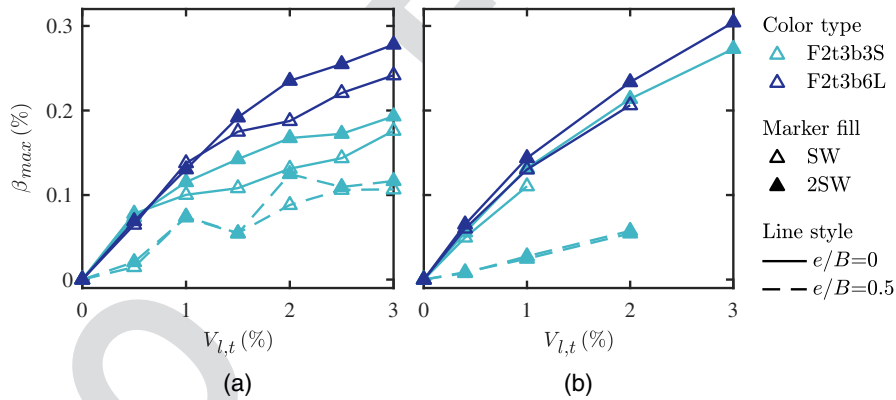
recorded. Several possible reasons could explain such behavior, ranging from experimental difficulties in guaranteeing a uniform soil density in the centrifuge, or the use of a soil mesh close to the footings that was not sufficiently fine and therefore incapable of describing the localized displacement gradients. For both the experiments and the simulations, the settlements under the footings appear relatively insensitive to the applied self-weight. Horizontal displacements predicted at the base of the raft foundation (see “Supplemental Materials”) are negligible for all investigated cases, similar to the results from the centrifuge tests. As such, most of the numerical simulations, similar to the experiments, are characterized by sliding at the soil-structure interface, progressively reducing in extension and intensity to zero as the stiffness and weight of the frame increases. A completely different pattern was found for the separate footing cases at $V_{l,t} = 1\%$ (Fig. 5): sliding at the soil-structure interface was never observed in the centrifuge nor predicted in the numerical analyses. Horizontal displacements are moderately lower than those obtained in greenfield conditions, showing local reductions directly beneath the footings. Only the eccentric case [Figs. 5(b and e)] provides deformations from both centrifuge data and numerical simulations that are slightly larger than in greenfield conditions, as the footings farther from the tunnel centerline were possibly dragged towards the nearer footings by the overall frame movement. The increase of volume loss, considered in “Supplemental Materials,” does not modify these observations, though a modest effect of structural weight can be detected and some slight slippage occurs under the central footings for the stiffer cases with $e/B = 0$ and nominal applied self-weight SW both in the experiments and in the simulations. Note that differential horizontal movements between footings are possible only when no ground floor slab or grade beam is present and infills are flexible.

464
465
466
467
468
469
470
471
472
473
474
475
476
477
478
479
480
481
482
483
484
485
486
487
488
489
490
491
492
493
494



F6:1

Fig. 6. Maximum frame distortion for rafts: (a) SW, centrifuge; (b) 2SW, centrifuge; (c) SW, numerical; and (d) 2SW, numerical.



F7:1

Fig. 7. Maximum frame distortion for separate footings: (a) centrifuge; and (b) numerical predictions.

495 Deformation Parameters

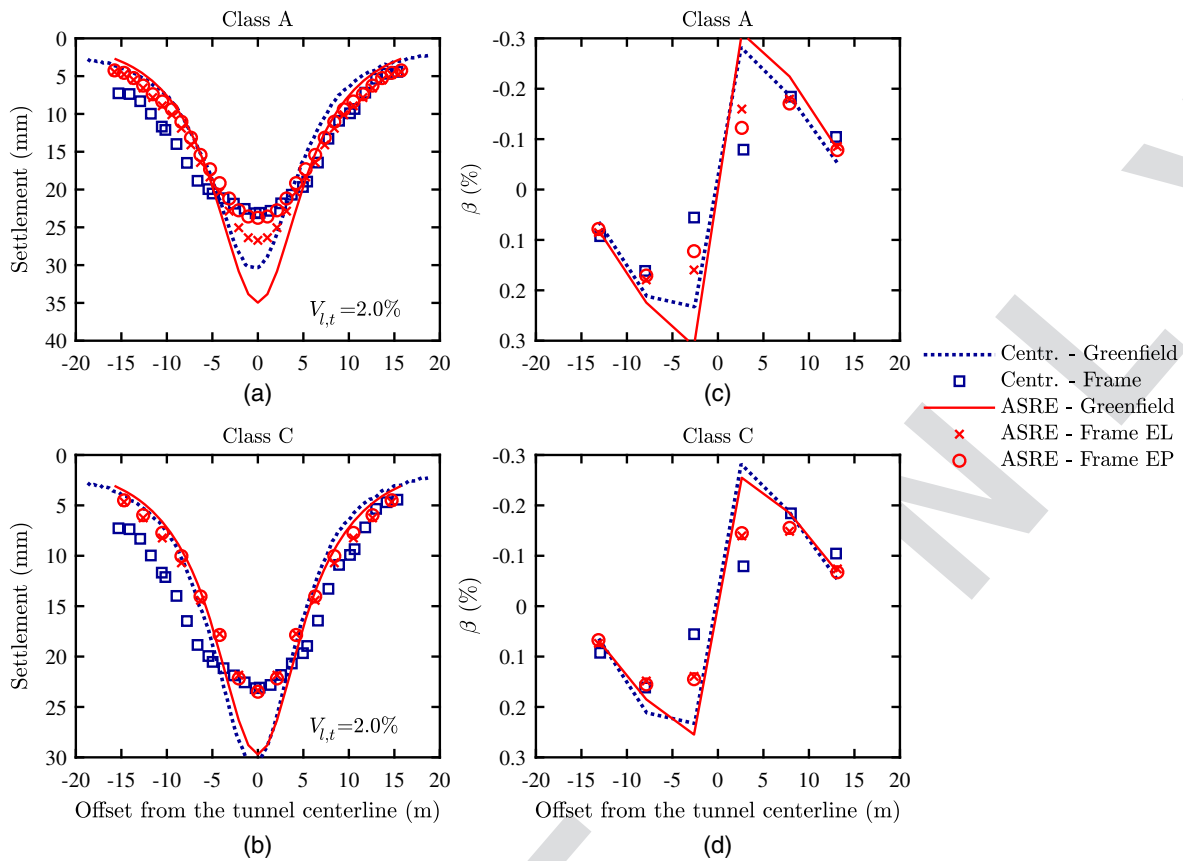
496 A concise representation of numerical results and their comparison
 497 with centrifuge data is provided in terms of maximum angular distortion
 498 β_{max} (sign was not considered) in Figs. 6 and 7 for rafts and
 499 separate footings, respectively, for $V_{l,t}$ up to 3%.

500 The overall trend outlined by the centrifuge results is well
 501 captured by the numerical predictions, especially for the analyses
 502 of frames founded on raft foundations, the β_{max} values being generally
 503 slightly overestimated in the numerical analyses. The β_{max}
 504 increases with $V_{l,t}$, with values lower than 0.3% for both rafts
 505 and separate footings. Eccentricity of the frame has a significant
 506 beneficial effect in limiting the structural distortion in comparison
 507 to the central configuration, while a detrimental influence can be
 508 observed for the building weight (i.e., 2SW analyses are always
 509 characterized by larger values of β_{max}).

Results of the Simplified Model

511 The performance of the simplified ASRE model for both linear
 512 elastic EL (perfect soil-foundation compatibility) and elastoplastic
 513 EP (with active sliders) conditions is compared with the centrifuge
 514 data of the *F2t3b6L* frame founded on the raft (for brevity, only this
 515 case is discussed here). Fig. 8 shows tunneling-induced settlements
 516 of the foundations and angular distortions of bays for central frames
 517 at $V_{l,t} = 2\%$. Horizontal raft displacements are not reported since
 518 they are nearly zero for the central frame cases, as previously discussed
 519 for the advanced modeling results.

520 First, the Class A predictions of the frame model in Figs. 8
 521 (a and c) are discussed. As noted earlier, these analyses were performed
 522 prior to collecting the centrifuge data to evaluate the accuracy of the
 523 two-stage model. In this ASRE analysis, despite the use of a greenfield
 524 input from Farrell et al. (2014) with slightly greater



F8:1 **Fig. 8.** Comparison of ASRE Classes A and C predictions with centrifuge results for frame *F2t3b6L*: (a and b) settlements; and (c and d) angular
 F8:2 distortions.

525 movements than Xu et al. (2020) [compare solid and dashed lines in
 526 Figs. 8(a and c)], the maximum building settlement was predicted
 527 well by the elastoplastic EP analysis, due to its capability of con-
 528 sidering gap formation, which is not allowed in the elastic EL case.
 529 The building settlement shape is also reproduced reasonably well
 530 by both the EL and EP analyses. This is confirmed by the compar-
 531 ison of the bay β values along the building length, with ASRE re-
 532 sults providing a satisfactory estimate of experimental outcomes,
 533 and only a marginal difference between EL and EP results.

534 Class C estimates, displayed in Figs. 8(b and d), are considered
 535 to evaluate the implications of using different greenfield inputs
 536 (the Class C greenfield input is directly applicable to the tunnel-
 537 frame interaction centrifuge results presented here). The difference
 538 in the foundation settlements between the EP and EL solutions is
 539 minimal when adopting the greenfield movements from Xu et al.
 540 (2020), indicating limited slider displacements for the EP case. The
 541 comparison between ASRE and experimental results in terms of
 542 maximum building settlement and β is also acceptable, as for
 543 the advanced FE model results.

544 Modification Factors

545 To synthesize data in design charts for use within preliminary risk
 546 assessments, this section provides angular distortion and horizon-
 547 tal strains at the foundation level using modification factors and
 548 recently proposed relative stiffness terms. To further populate the
 549 dataset of eccentric structures with relatively high frame flexibility,
 550 additional numerical analyses were run with the advanced FE
 551 model using an enlarged mesh, required to accommodate the full

552 length of the long eccentric frames (e.g., cases *F2t3b3L* and
 553 *F2t3b6L* for $e/B = 0.5$). Furthermore, the ASRE model was used
 554 to simulate all frames in Table 1 under central and eccentric con-
 555 ditions ($e/B = 0; 0.5$) using the elastoplastic EP analysis method.
 556 Also note that results computed at $V_{l,t} = 1$ and 2% are considered
 557 for the advanced FE model and centrifuge results, whereas only
 558 $V_{l,t} = 2\%$ is selected for ASRE considering that, for the simplified
 559 method, there is a limited effects of $V_{l,t}$.

560 Modification factors for the angular distortion, M^β , derived
 561 from all the advanced and ASRE numerical analyses are plotted
 562 in Figs. 9 and 10 against the relative soil-structure stiffness param-
 563 eter κ for the raft and separate footings cases, respectively. Values
 564 of β refer to panels confined by two slabs and two columns, while
 565 horizontal strains due to differential horizontal displacements of
 566 separate footing are not accounted for. These data are compared on
 567 the same charts with the corresponding centrifuge test values and
 568 with the empirical upper and lower envelopes (based on centrifuge
 569 test data) proposed by Xu et al. (2020, 2021).

570 Fig. 9 indicates that, for raft foundations, all the numerical
 571 results fit relatively well within the empirical envelopes for both
 572 the centered and eccentric frames. For each examined case with
 573 $e/B = 0$, both FE predictions yield a somewhat larger distortion
 574 for a given maximum ground slope, the difference between experi-
 575 mental and numerical values being larger for the more flexible
 576 cases. In contrast, for $e/B = 0.5$, Abaqus numerical data points
 577 tend to concentrate near the lower envelope for the eccentric frames
 578 on raft foundations. Also, the ASRE simulations indicate a rate of
 579 variation of M^β against relative stiffness κ that is lower than the
 580 empirical envelopes.

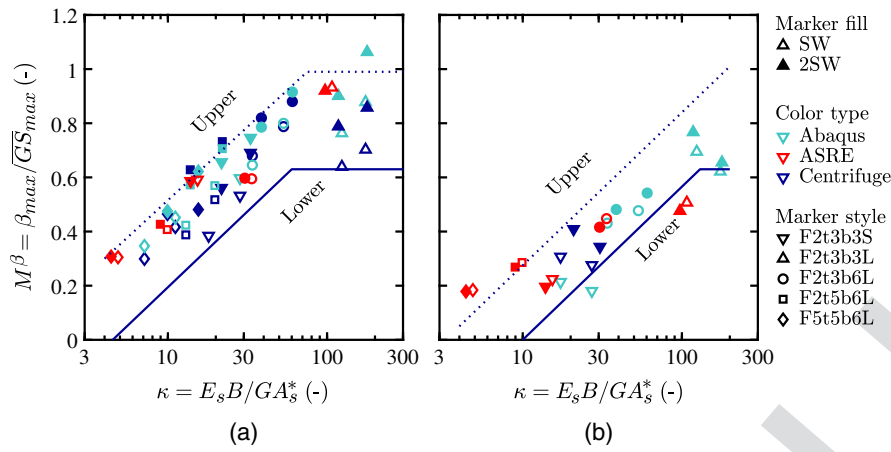


Fig. 9. Modification factor of angular distortion for rafts: (a) central; and (b) eccentric tunnels. (Envelope data from Xu et al. 2020.)

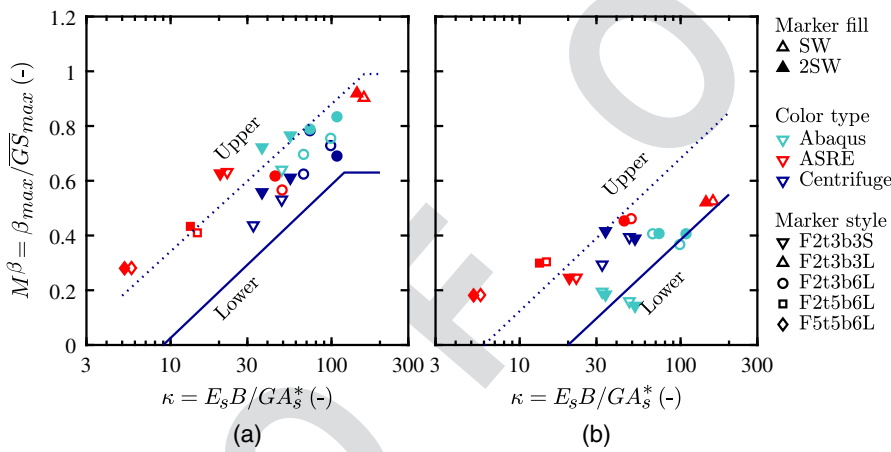


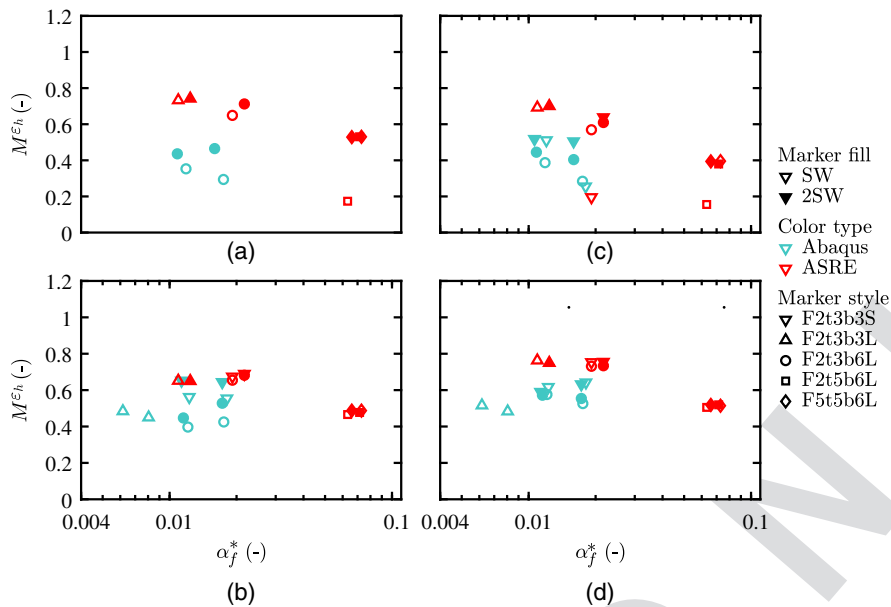
Fig. 10. Modification factor of angular distortion for footings: (a) central; and (b) eccentric tunnels. (Envelope data from Xu et al. 2021.)

As seen in Fig. 10, there is agreement between experimental and numerical factors for frames with separate footings, with the numerical data points tending to be located close to the upper envelope for $e/B = 0$. Similar to the case of the raft foundation, the agreement between ASRE and advanced results are less good for the eccentric frames on separate footings than they are for the centered frames. This may be partly due to the way that eccentric frames affect the tunneling-induced arching mechanism, which is not considered by the elastic continuum used in the ASRE model.

Overall, numerical results confirm that the envelopes proposed by Xu et al. (2020, 2021) are reasonable for a wider range of scenarios. Also, Figs. 9 and 10 allow for a direct comparison between advanced and ASRE predictions in terms of normalized angular distortions, indicating a good agreement except for relatively flexible eccentric frames. This difference for flexible eccentric frames occurred as a result of the building weight effect, which slightly increases tunneling-induced settlements, a mechanism not considered by ASRE.

To illustrate the influence of bay relative stiffness and building eccentricity on horizontal deformations, numerical results of the modification factor for horizontal strains M^{ϵ_h} obtained from advanced and simplified models are compared in Fig. 11. In this figure, values of M^{ϵ_h} were computed from the maximum differential

horizontal displacements of greenfield and building displacement profiles at the footing locations. Centrifuge results are not considered because of the previously mentioned effects of welding on the horizontal displacements of the footings (Xu et al. 2021). Interestingly, both models predicted horizontal modification factors M^{ϵ_h} lower than unity in both compression and tension (i.e., a semiflexible behavior), with no clear trends associated with the change in eccentricity e/B . For a given frame and location, the reduction in the building self-weight slightly reduced the horizontal deformations in the advanced model for all cases, while its impact on ASRE results is significant in compression for the eccentric two story frames that are relatively stiff in shear (namely, $F2t3b3S$ and $F2t5b6L$). More importantly, in most cases the level of predicted normalized horizontal deformation in the advanced approach is notably lower than that resulting from the ASRE predictions, likely due to the former model accounting for the ground stiffness degradation related to the footing restraint action in the horizontal direction, as displayed in Fig. 5. Finally, considering the full parametric study conducted with ASRE, the decrease in M^{ϵ_h} with the relative stiffness α_f^* is notable only when the cross-sectional thickness is increased, resulting in values of α_f^* being greater by approximately one order of magnitude.



F11:1 **Fig. 11.** Modification factor of horizontal strains at the footings obtained from numerical models: (a) tensile and (b) compressive strains for central
 F11:2 structures; and (c) tensile and (d) compressive strains for eccentric tunnels.

626 Conclusions

627 The paper describes a numerical study intended to verify the capa-
 628 bilities of numerical approaches, characterized by different levels of
 629 complexity, in reproducing the response of bare frame buildings to
 630 tunneling in sand, as observed during centrifuge tests considering
 631 both raft foundations and separate footings. Numerical modeling
 632 was also used to expand the available centrifuge dataset by analyz-
 633 ing additional eccentric cases.

634 The numerical models, all based on the FEM, were established
 635 with two aims: on one side, executing advanced simulations of the
 636 interaction problem by explicitly including the tunnel, the soil, and
 637 the frame with its foundation; on the other side, developing more
 638 simplified tools for the engineering practice, without the need of
 639 running time-consuming analyses and of adopting advanced con-
 640 stitutive models. The latter are two-stage models in which the frame
 641 is modeled through a frame consisting of beams, the soil is substi-
 642 tuted by coupled springs with optional plastic sliders at the soil-
 643 structure interface, while tunneling is input in terms of greenfield
 644 movements. In both the advanced and simplified FE models, the
 645 behavior at the soil-building interface can be specifically accounted
 646 for by limiting the allowable tangential stress and by setting the
 647 tensile strength to zero.

648 Both the discussed numerical approaches were able to capture
 649 settlements and angular distortions of the frame bays for both rafts
 650 and separate footings. The accuracy of the advanced numerical
 651 model can be attributed to various factors: a proper, even if simpli-
 652 fied, simulation of tunnel excavation; the use of an advanced
 653 constitutive law for the sand, the capability of correctly repro-
 654 ducing the tunneling-induced subsidence throughout a relatively
 655 large range of volume loss values, over 2%; and the use of contact
 656 laws to allow for the occurrence of sliding and the formation of
 657 a gap below the frame foundation, as observed experimentally.
 658 Notably, it was demonstrated that good and quick estimates of
 659 settlements and building distortions can be achieved for framed
 660 structures with the simplified ASRE model; these can subsequen-
 661 tly be refined when more representative greenfield data become
 662 available.

663 Approximated approaches for the estimation of both bending
 664 and shear stiffness were presented and validated. The whole set
 665 of numerical results was interpreted in terms of modification fac-
 666 tors for both angular distortion and horizontal strain in relation
 667 to relative soil-building stiffness. These angular distortion results
 668 agreed well with previously proposed empirical envelopes (Xu
 669 et al. 2020, 2021), defined on the basis of centrifuge outcomes,
 670 that can bind, with reasonable success, the range of predicted
 671 angular distortions, considering the impact of foundation type
 672 (i.e., raft or separate footings) and relative soil-structure stiff-
 673 ness. Additionally, indications were given on expected ranges of hori-
 674 zontal strains caused by the differential horizontal displacements
 675 between separate footings. Numerical results confirmed that shear
 676 deformations play an important role for all considered buildings,
 677 whereas only frames on separate footings are sensitive to horizontal
 678 ground movements.

679 The envelopes of modification factors may be of use for a pre-
 680 liminary assessment of the reduction of bay angular distortion in
 681 comparison to the greenfield case. Alternatively, the simplified
 682 numerical approach represents a viable tool for a prompt pre-
 683 liminary assessment, which also accounts for many important
 684 structural characteristics that are not considered in the proposed
 685 envelopes (e.g., bay length-to-height ratio, different stiffness of
 686 columns and floors).

687 In this paper no explicit structural model of the infills was con-
 688 sidered, which may have a significant impact on the response of the
 689 frame due to their stiffening effect. Therefore, the obtained results
 690 and current assessment procedures are deemed conservative if ap-
 691 plied within the context of tunneling beneath infilled frames. Future
 692 work will provide further insights into both the stiffening action as
 693 well as the deformations of infills of framed buildings.

694 Data Availability Statement

695 Data and models are available from the corresponding author on
 696 request.

697 Acknowledgments

698 This project has received funding from the European Union's
699 Horizon 2020 research and innovation programme under the Marie
700 Skłodowska-Curie Grant Agreement No. 793715. The financial
701 support provided by the China Scholarship Council (CSC) and
702 the University of Nottingham, UK, is also recognized.

703 Supplemental Materials

704 Figs. S1–S8 and Tables S1 and S2 are available online in the ASCE
705 Library (www.ascelibrary.org).

706 References

707 Amorosi, A., D. Boldini, G. De Felice, M. Malena, and M. Sebastianelli.
708 2014. "Tunnelling-induced deformation and damage on historical
709 masonry structures." *Géotechnique* 64 (2): 118–130. <https://doi.org/10.1680/geot.13.P.032>.
710
711 Boldini, D., N. Losacco, S. Bertolin, and A. Amorosi. 2018. "Finite
712 Element modelling of tunnelling-induced displacements on framed
713 structures." *Tunnelling Underground Space Technol.* 80 (Oct): 222–231.
714 <https://doi.org/10.1016/j.tust.2018.06.019>.
715 Boone, S. J. 1996. "Ground-movement-related building damage."
716 *J. Geotech. Eng.* 122 (11): 886–896. [https://doi.org/10.1061/\(ASCE\)0733-9410\(1996\)122:11\(886\)](https://doi.org/10.1061/(ASCE)0733-9410(1996)122:11(886)).
717
718 Boscardin, M. D., and E. J. Cording. 1989. "Building response to
719 excavation-induced settlement." *J. Geotech. Eng.* 115 (1): 1–21.
720 [https://doi.org/10.1061/\(ASCE\)0733-9410\(1989\)115:1\(1\)](https://doi.org/10.1061/(ASCE)0733-9410(1989)115:1(1)).
721 Burland, J. B., B. B. Broms, and V. F. B. De Mello. 1977. "Behaviour of
722 foundations and structures." In Vol. 2 of *Proc., 9th Int. Conf. on Soil
723 Mechanics and Foundation Engineering*, 495–546. Tokyo.
724 Burland, J. B., and C. P. Wroth. 1974. "Settlement of buildings and
725 associated damage." In *Proc., Conf. on Settlement of Structures*,
726 611–654. London: Pentech Press.
727 Cheng, C. Y., G. R. Dasari, Y. K. Chow, and C. F. Leung. 2007. "Finite
728 element analysis of tunnel-soil-pile interaction using displacement
729 controlled model." *Tunnelling Underground Space Technol.* 22 (4):
730 450–466. <https://doi.org/10.1016/j.tust.2006.08.002>.
731 Comodromos, E. M., M. C. Papadopoulou, and G. K. Konstantinidis. 2014.
732 "Numerical assessment of subsidence and adjacent building move-
733 ments induced by TBM-EPB tunneling." *J. Geotech. Geoenviron. Eng.*
734 140 (11): 04014061. [https://doi.org/10.1061/\(ASCE\)GT.1943-5606.0001166](https://doi.org/10.1061/(ASCE)GT.1943-5606.0001166).
735
736 Cook, D. 1994. "Studies of settlement and crack damage in old and
737 new facades." In Vol. 6 of *Proc., 3rd Int. Masonry Conf.*, 203–211.
738 Cowper, G. R. 1966. "The shear coefficient in Timoshenko's beam theory."
739 *J. Appl. Mech.* 33 (2): 335–340. <https://doi.org/10.1115/1.3625046>.
740 Dafalias, Y. F., and M. T. Manzari. 2004. "Simple plasticity sand model
741 accounting for fabric change effects." *J. Eng. Mech.* 130 (6): 622–634.
742 [https://doi.org/10.1061/\(ASCE\)0733-9399\(2004\)130:6\(622\)](https://doi.org/10.1061/(ASCE)0733-9399(2004)130:6(622)).
743 Dimmock, P. S., and R. J. Mair. 2008. "Effect of building stiffness on
744 tunnelling-induced ground movement." *Tunnelling Underground Space
745 Technol.* 23 (4): 438–450. <https://doi.org/10.1016/j.tust.2007.08.001>.
746 Elkayam, I., and A. Klar. 2019. "Nonlinear elasto-plastic formulation for
747 tunneling effects on superstructures." *Can. Geotech. J.* 56 (7): 956–969.
748 <https://doi.org/10.1139/cgj-2018-0021>.
749 Fargnoli, V., D. Boldini, and A. Amorosi. 2015a. "Twin tunnel excavation
750 in coarse grained soils: Observations and numerical back-predictions
751 under free field conditions and in presence of a surface structure."
752 *Tunnelling Underground Space Technol.* 49 (Jun): 454–469. <https://doi.org/10.1016/j.tust.2015.06.003>.
753
754 Fargnoli, V., C. G. Gragnano, D. Boldini, and A. Amorosi. 2015b.
755 "3D numerical modelling of soil-structure interaction during EPB
756 tunnelling." *Géotechnique* 65 (1): 23–37. <https://doi.org/10.1680/geot.14.P.091>.
757
758 Farrell, R. 2010. "Tunnelling in sands and the response of buildings."
759 Ph.D. thesis, Cambridge Univ.

Farrell, R., R. Mair, A. Sciotti, and A. Pigorini. 2014. "Building response to
tunnelling." *Soils Found.* 54 (3): 269–279. <https://doi.org/10.1016/j.sandf.2014.04.003>.
Finno, R. J., F. T. Voss, E. Rossow, and J. T. Blackburn. 2005. "Evaluating
damage potential in buildings affected by excavations." *J. Geotech.
Geoenviron. Eng.* 131 (10): 1199–1210. [https://doi.org/10.1061/\(ASCE\)1090-0241\(2005\)131:10\(1199\)](https://doi.org/10.1061/(ASCE)1090-0241(2005)131:10(1199)).
Franza, A., S. Acikgoz, and M. J. DeJong. 2020. "Timoshenko beam
models for the coupled analysis of building response to tunnelling."
Tunnelling Underground Space Technol. 96 (Feb): 103160. <https://doi.org/10.1016/j.tust.2019.103160>.
Franza, A., and M. J. DeJong. 2019. "Elastoplastic solutions to predict
tunneling-induced load redistribution and deformation of surface
structures." *J. Geotech. Geoenviron. Eng.* 145 (4): 04019007. [https://doi.org/10.1061/\(ASCE\)GT.1943-5606.0002021](https://doi.org/10.1061/(ASCE)GT.1943-5606.0002021).
Franzius, J. N., D. M. Potts, and J. B. Burland. 2006. "The response of
surface structures to tunnel construction." *Proc. Inst. Civ. Eng. Geotech.
Eng.* 159 (1): 3–17. <https://doi.org/10.1680/geng.2006.159.1.3>.
Fu, J., Z. Yu, S. Wang, and J. Yang. 2018. "Numerical analysis of
framed building response to tunnelling induced ground movements."
Eng. Struct. 158 (Mar): 43–66. <https://doi.org/10.1016/j.engstruct.2017.11.039>.
Giardina, G., N. Losacco, M. J. DeJong, G. M. B. Viggiani, and R. J. Mair.
2020. "Effect of soil models on the prediction of tunnelling-induced
deformations of structures." *Proc. Inst. Civ. Eng. Geotech. Eng.*
173 (5): 379–397. <https://doi.org/10.1680/jgeen.18.00127>.
Goh, K. H., and R. J. Mair. 2014. "Response of framed buildings to
excavation-induced movements." *Soils Found.* 54 (3): 250–268. <https://doi.org/10.1016/j.sandf.2014.04.002>.
Haji, T. K., A. M. Marshall, and W. Tizani. 2018. "A cantilever approach
to estimate bending stiffness of buildings affected by tunnelling."
Tunnelling Underground Space Technol. 71 (Jan): 47–61. <https://doi.org/10.1016/j.tust.2017.08.005>.
Lambe, T. W. 1973. "Predictions in soil engineering." *Géotechnique* 23 (2):
151–202. <https://doi.org/10.1680/geot.1973.23.2.151>.
Lehane, B., and E. Cosgrove. 2000. "Applying triaxial compression stiffness
data to settlement prediction of shallow foundations on cohesionless
soil." *Proc. Inst. Civ. Eng. Geotech. Eng.* 143 (4): 191–200. <https://doi.org/10.1680/geng.2000.143.4.191>.
Losacco, N., A. Burghignoli, and L. Callisto. 2014. "Uncoupled evaluation
of the structural damage induced by tunnelling." *Géotechnique* 64 (8):
646–656. <https://doi.org/10.1680/geot.13.P.213>.
Losacco, N., L. Callisto, and A. Burghignoli. 2016. "Soil-structure interac-
tion due to tunnelling in soft ground, an equivalent solid approach."
In *Proc., Structural Analysis of Historical Constructions: Anamnesis,
Diagnosis, Therapy, Controls*, edited by K. Van Balen and E. Verstryngne,
495–501. Boca Raton, FL: CRC Press.
Mair, R. 2013. "Tunnelling and deep excavations: Ground movements
and their effects." In *Proc., 15th European Conf. on Soil Mechanics
and Geotechnical Engineering—Geotechnics of Hard Soils—Weak
Rocks (Part 4)*, edited by A. Anagnostopoulos, M. Pachakis, and
C. Tsatsanifos, 39–70. Amsterdam, Netherlands: IOS Press.
Mair, R. J., R. N. Taylor, and A. Bracegirdle. 1993. "Subsurface settlement
profiles above tunnels in clay." *Géotechnique* 43 (2): 315–320. <https://doi.org/10.1680/geot.1993.43.2.315>.
Mair, R. J., R. N. Taylor, and J. B. Burland. 1996. "Prediction of
ground movements and assessment of risk of building damage due
to bored tunnelling." In *Proc., Int. Symp. Geotechnical Aspects of
Underground Construction in Soft Ground*, edited by R. J. Mair and
R. N. Taylor, 713–718. Rotterdam, Netherlands: A.A. Balkema.
Marshall, A. M., A. Klar, and R. J. Mair. 2010. "Tunneling beneath
buried pipes: View of soil strain and its effect on pipeline behavior."
J. Geotech. Geoenviron. Eng. 136 (12): 1664–1672. [https://doi.org/10.1061/\(ASCE\)GT.1943-5606.0000390](https://doi.org/10.1061/(ASCE)GT.1943-5606.0000390).
Namazi, E., and H. Mohamad. 2013. "Assessment of building damage in-
duced by three-dimensional ground movements." *J. Geotech. Geoenviron.
Eng.* 139 (4): 608–618. [https://doi.org/10.1061/\(ASCE\)GT.1943-5606.0000822](https://doi.org/10.1061/(ASCE)GT.1943-5606.0000822).
Pickhaver, J., H. Burd, and G. Houslyby. 2010. "An equivalent beam
method to model masonry buildings in 3D finite element analysis."

- 830 *Comput. Struct.* 88 (19): 1049–1063. <https://doi.org/10.1016/j.compstruc>
831 [.2010.05.006](https://doi.org/10.1016/j.compstruc.2010.05.006).
- 832 Potts, D. M., and T. I. Addenbrooke. 1997. “A structure’s influence on
833 tunnelling-induced ground movements.” *Proc. Inst. Civ. Eng. Geotech.*
834 *Eng.* 125 (2): 109–125. <https://doi.org/10.1680/igeng.1997.29233>.
- 835 Rampello, S., L. Callisto, G. Viggiani, and F. M. Soccodato. 2012.
836 “Evaluating the effects of tunnelling on historical buildings: The
837 example of a new subway in Rome/Auswertung der Auswirkungen
838 des Tunnelbaus auf historische Gebäude am Beispiel einer neuen
839 U-Bahnlinie in Rom.” *Geomech. Tunnelling* 5 (3): 275–299. [https://doi](https://doi.org/10.1002/geot.201200017)
840 [.org/10.1002/geot.201200017](https://doi.org/10.1002/geot.201200017).
- 841 Ritter, S., G. G. Giardina, A. Franza, and M. J. DeJong. 2020. “Building
842 deformation caused by tunneling: Centrifuge modeling.” *J. Geotech.*
843 *Geoenviron. Eng.* 146 (5): 04020017. [https://doi.org/10.1061/\(ASCE\)GT](https://doi.org/10.1061/(ASCE)GT.1943-5606.0002223)
844 [.1943-5606.0002223](https://doi.org/10.1061/(ASCE)GT.1943-5606.0002223).
- 845 Son, M., and E. J. Cording. 2005. “Estimation of building damage due to
846 excavation-induced ground movements.” *J. Geotech. Geoenviron. Eng.*
131 (2): 162–177. [https://doi.org/10.1061/\(ASCE\)1090-0241\(2005\)](https://doi.org/10.1061/(ASCE)1090-0241(2005)131:2(162))
131:2(162).
- Visone, C. 2008. “Performance-based approach in seismic design of
embedded retaining walls.” Ph.D. thesis, Univ. Naples Federico II. **16** 850
- Xu, J., A. Franza, and A. M. Marshall. 2020. “Response of framed
buildings on raft foundations to tunneling.” *J. Geotech. Geoenviron.*
Eng. 146 (11): 04020120. [https://doi.org/10.1061/\(ASCE\)GT.1943-5606](https://doi.org/10.1061/(ASCE)GT.1943-5606.0002376)
852 [.0002376](https://doi.org/10.1061/(ASCE)GT.1943-5606.0002376). 853
- Xu, J., A. Franza, A. M. Marshall, N. Losacco, and D. Boldini. 2021.
854 “Tunnel-framed building interaction: Comparison between raft and
855 separate footing foundations.” *Géotechnique* 71 (7): 631–644. [https://](https://doi.org/10.1680/jgeot.19.P.393)
856 doi.org/10.1680/jgeot.19.P.393. 857
- Yiu, W. N., H. J. Burd, and C. M. Martin. 2017. “Finite-element modelling
858 for the assessment of tunnel-induced damage to a masonry building.”
859 *Géotechnique* 67 (9): 780–794. [https://doi.org/10.1680/jgeot.sip17.P](https://doi.org/10.1680/jgeot.sip17.P.249)
860 [.249](https://doi.org/10.1680/jgeot.sip17.P.249). 861
- Zhao, Y. 2008. “In situ soil testing for foundation performance prediction.”
862 Ph.D. thesis, Cambridge Univ. **17** 864

Queries

1. Please provide the ASCE Membership Grades for the authors who are members.
2. The title has been changed. Please verify.
3. Please provide author titles (e.g., Professor, Director) and postal codes for all affiliation footnotes.
4. Please check the hierarchy of section heading levels.
5. ASCE Open Access: Authors may choose to publish their papers through ASCE Open Access, making the paper freely available to all readers via the ASCE Library website. ASCE Open Access papers will be published under the Creative Commons-Attribution Only (CC-BY) License. The fee for this service is USD 2,000 and must be paid prior to publication. If you indicate Yes, you will receive a follow-up message with payment instructions. If you indicate No, your paper will be published in the typical subscribed-access section of the Journal. After a journal article is published, its copyright status cannot change until two years have passed. For further information, please see <https://ascelibrary.org/page/openaccessoptionsandrights>.
6. The citation Xu et al. (2020a) has been changed to Xu et al. (2020) to match with the reference list.
7. The citation Xu et al. (2020b) has been changed to Xu et al. (2021) to match with the reference list.
8. Please check all figures, figure citations, and figure captions to ensure they match and are in the correct order.
9. ASCE style for math is to set all mathematical variables in italic font. Please check all math variables throughout the paper, both in equations and throughout the text, to ensure all conform to ASCE style.
10. Insert space before “GPa.”
11. Insert space before “MPa.”
12. Please check and verify whether to (i) should be changed to (a) or to delete it.
13. Please provide the publisher or sponsor name and location (not the conference location) for Burland et al. (1977).
14. Please provide the publisher or sponsor name and location (not the conference location) for Cook (1994).
15. Please provide the department name for Farrell (2010).
16. Please provide the department name for Visone (2008).
17. Please provide the department name for Zhao (2008).